Finite-Element Simulations of Elastoplastic Flow during Compression of a Sample in a Diamond Anvil Cell under Extremely High Pressure: Effects of Geometry and Material Properties

Biao Feng and Valery I. Levitas

Finite element simulations of elastoplastic flow during compression of a sample in a diamond anvil cell under extreme high pressures: Effects of geometry and material properties

Biao Feng[1]   and   Valery I. Levitas[2,*]

[1]*Los Alamos National Laboratory, Los Alamos, NM 87545, United States*

[2]*Departments of Aerospace Engineering, Mechanical Engineering, and Material Science and Engineering, Iowa State University, Ames, IA 50011, United States*

Abstract   Finite element simulations are conducted to investigate large elastoplastic deformations of rhenium under multi-megabar pressures in a diamond anvil cell (DAC), with an emphasis on the effects of geometric and material properties. The following published experimental phenomena have been reproduced: (1) the pressure distribution at the sample/diamond contact surface and the final sample thickness at pressure up to 300 GPa; (2) the cupping (i.e. appearance of a cup-like concave shape of the contact diamond-sample surface) and double cupping phenomena at megabar pressures; (3) three stages at the curve of the maximum pressure versus compressive force; (4) stages of material flow with increasing load; (5) pressure drop at the periphery after cupping in that region, and (6) change in direction of material flow to the center without change in the sign of the pressure gradient. The effect of the culet geometry, bevel angle, sample thickness, and sample/gasket system are analyzed in detail. The obtained results improve the understanding of the material mechanical response under extreme pressures

---

[*] Corresponding author.
Email address for Valery Levitas: vlevitas@iastate.edu
Email address for Biao Feng: fengbiao11@gmail.com

and large elastoplastic deformations and are beneficial for the optimum design of DAC with the goal of reaching the high and record high pressures once or multiple times.

Keywords: High pressure, Diamond anvil cells, Plasticity, Finite element method, Geometric properties, Yield strength

I.   INTRODUCTION

By compressing a sample between two diamond anvils in a diamond anvil cell (DAC), static megabar pressures are generated in experiments [1-5]. To find new physical phenomena and new materials, the pressure level need to be increased; meanwhile, anvils should not break during single or multiple experimental runs. As an important example, we refer to the recent discussion in *Science* [6-8]: Metallic hydrogen was obtained in [6] under a pressure of 495 GPa. It was stated in a critical comment [7] that 96% of diamonds failed while attempting to reach 350 GPa; in particular, the method of estimation of pressure based on the applied force used in [6] was criticized. The response [8] asserted that the achievable pressure strongly depends on the geometry of the anvil, the thickness of the gasket, and the degree of cupping of the diamond (i.e. appearance of a cup-like concave shape of the contact diamond-sample surface). A very detailed experimental study of the pressure distribution and deformation of an anvil and sample in the megabar pressure range was presented in [3] and [9].

Numerical modeling of the compression of a sample in DAC is related to significant theoretical and computational problems due to multiple physical, geometric, and contact nonlinearities. Geometric nonlinearity is related to large elastic and plastic deformations, material rotations, and displacements. Physical nonlinearities are caused by nonlinear elasticity rules, the plasticity of the sample, and the pressure-dependence of the yield strength. Contact

2

nonlinearities are due to the deformed surfaces and contact relative sliding with unknown sliding and cohesion zones. Reaching convergence of the solution to the actual one for such complex problems requires significant algorithmic efforts; however, these will not be discussed here.

The finite element method (FEM) is widely used to study the stress-strain states of the sample and anvils in DAC [10-17]. Moss *et al.* found by FEM that the increase in the yield strength of a gasket plays the key role in achieving extreme high pressure [10]. They claimed to have achieved the pressure of 460 GPa experimentally by using a metal gasket with yield strength of 2.5 GPa. Moss and Goettel performed finite element analyses of beveled diamond anvils and discussed the design of a diamond anvil by changing culet geometries [11]. Merkel *et al*. [13] extended previous FEM calculations [10, 11] to simulate the experiment on compression of a rhenium sample up to 300 GPa [3] and to numerically study the effects of the geometric parameters of the sample and anvil system [15]. Coupled plastic flows and strain-induced phase transforms in the sample in DAC [18-20] and rotational DAC (RDAC) [21-23] were investigated, with assumptions of the sample with small elastic and transformational strains and the diamond anvils as a rigid body.

Previous models [10-13, 15] were not based on a fully large-strain framework and were therefore unable to quantitatively reproduce experimental results (e.g. pressure distribution and sample thickness) under the extreme condition of several-megabar pressures. In most of these works, equations were not given and results of simulations using some available FEM codes were presented. Feng *et al*. [14, 24] recently formulated a thermodynamically-consistent system of equations considering large elastic and plastic deformations of a sample and large elastic deformation of the diamond anvil. With FEM, we successfully reproduced the experimental pressure distribution [3] at pressure up to 300 GPa. We also numerically revealed a pressure self-

3

focusing effect [16, 24], which allows one to achieve an extremely large pressure gradient and, consequently, high pressure at the center of a sample. These studies were extended on a 3D problem on compression and torsion of a sample in RDAC under extreme pressures [16, 24].

It is necessary to note that many material properties used in simulations, such as pressure-dependent yield strength and higher-order elastic constants, as well as the friction coefficient, are not known from experiments. Their determination in the process of fitting numerical solutions to the experimental distributions represents a significant additional challenge.

It is well known that geometric and material properties are essential to the determination of material responses under extreme high pressure. The use of *beveled* diamond anvils in DAC is the key to generating static pressures above 1 Megabar [5, 25]. Experimentally, however, the choice of the bevel angle is expensive due to fracture of one or both anvils [11]. Consequently, the FEM simulations are important for optimization of the geometry. In addition, because the introduction of a gasket into a DAC is a milestone in the history of DAC [25], the study of the system of a gasket and sample under megabar pressures by using FEM is very important. However, this was not done in previous work.

In this paper, we study the effects of geometric and material properties in DAC based on the advanced large deformation framework developed in [14, 24]. A total system of equations is presented in Section II. Stresses and plastic flow for the culler radius $R = 5 \mu m$, bevel angle $\alpha = 8.5^\circ$, and initial sample thickness $h_0 = 20 \mu m$ are studied in Section III.B. In particular, experimental pressure distribution [3], double cupping (i.e. the appearance of two cup-like concave parts at the diamond/sample surface) [9], and cupping-related pressure drop [3, 9] were reproduced numerically. The transition from plastic flow from the center, to partial flow to the

center, and then to elastic deformation, observed experimentally under increased loading in [3,9], is reproduced. Deformation of the diamond anvil plays a crucial role in this phenomenon. It also explains why the friction stress and pressure gradient do not change sign when the velocity changes sign: because the relative sliding velocity with respect to diamond is either zero or positive. The effect of the diamond flat tip radius (the flat part at the center of the sample and diamond contact surface) is studied in Section III.C. By using the third-order elastic constants from [26], the cupping at the pressure of 300 GPa in experiments [3] was not reproduced in our previous simulations [14]. Thus, we artificially adjusted the third-order elastic constants in [14] to reproduce cupping. We found here that this discrepancy was caused by the absence of the flat part of the diamond in the previous simulations [14]. Here, with the flat diamond tip, we reproduced both pressure distribution and cupping by using the third-order elastic constants from [26]. We also obtained double cupping, which was observed in recent experiments [9]. The effect of the bevel angle is analyzed in Section III.D. Increasing the bevel angle increases the pressure gradient, pressure, and cupping at the center, but reduces cupping at the periphery. It is shown in Section III.E that the increase in sample thickness reduces the pressure gradient and pressure at the initial compression stage. This effect decreases and disappears at large compression. The sample-and-gasket system is treated for extreme pressures for the first time in Section III.F. Thus, in a small sample whose yield strength is twice as small at zero pressure as the yield strength of the gasket, the reduction in pressure is relatively small and the change in pressure distribution in the gasket is negligible. Section IV contains concluding remarks. The obtained results improve the understanding of the material mechanical responses under extreme conditions of high pressures and plastic deformations and are beneficial for the optimum design of a DAC system.

II. PROBLEM FORMULATION

### II.A. Geometry and boundary conditions

A schematic of a DAC is shown in Fig. 1a, where a normal stress σ_n is applied on the diamond surface and a sample is compressed by two diamond anvils. We ignore the anisotropy of the diamond anvil in the circumferential direction to use an axisymmetric formulation. Due to the axisymmetric loads and geometry of DAC and the symmetry with respect to the horizontal plane *IJ* in Fig. 1c, we consider a quarter of DAC as shown in Fig. 1b. The major geometric parameters for an anvil and for the contact surface between diamond and the sample are given in Figs. 1b and 1c, respectively. The geometry of the preindented sample is shown, along with the magnified central part, in Fig. 1c. One half of the sample thickness at *r*=0 in the initial undeformed configuration is $h_0/2$ (line *CI* in Fig. 1c). The undeformed shape of the contact surface is as follows: from point *C* at *r*=0 to point *R*, there is a small flat region with the radius r_0; from point *R* to point *G*, the contact surface is inclined with an initial bevel angle α; at the periphery line, *GE* has an inclined angle 43.27°; the radial distance between *CG* is $150\,\mu m$; the radial distance *IJ* at the symmetry plane is $772.5\,\mu m$, which is long enough to exclude the boundary effect of the right end *HJ*; and the thickness of the boundary *HJ* is $125\,\mu m$. We will discuss the effects of geometric parameters by varying h_0, r_0, and α in the range achievable experimentally.

The boundary conditions for a quarter of DAC in Fig. 2b are listed as follows:

(1) In experiments, an axial force Q is applied to the diamonds. In simulations, the homogeneous normal stress σ_n is applied at the top surface *AB* of the DAC (as also shown

6

in Fig. 1a). Because σ_n is only several GPa and simulations show that the deformation of anvil is negligible at AB, the total compressive force Q is σ_n multiplied by the area of the top surface of the anvil $\pi(1.05\,\text{mm})^2$. Preliminary calculations showed that stresses in the sample and at the tip of the diamond are independent of the possible heterogeneity of the distribution of σ_n at the surface AB.

(2) At the z-axis (the symmetry axis $r = 0$) (line AC for the anvil in Fig. 1b and line CI for the sample in Fig. 1c), the shear stress τ_{rz} and radial displacement u_r are zero.

(3) The Coulomb friction model is applied at the contact surface ($CRGE$ shown in Fig. 1c). Slipping is allowed when the friction stress reaches $\mu\sigma_c$ (σ_c is the normal contact stress at the contact surface between the diamond and the sample, and μ is the Coulomb friction coefficient). Otherwise, the cohesion condition, i.e. continuity of displacements, is applied. At the symmetry plane $z = 0$ (plane IJ in Fig. 1c), the radial shear stress $\tau_{rz} = 0$ and the axial displacement $u_z = 0$.

(4) Other surfaces not mentioned above are stress-free.
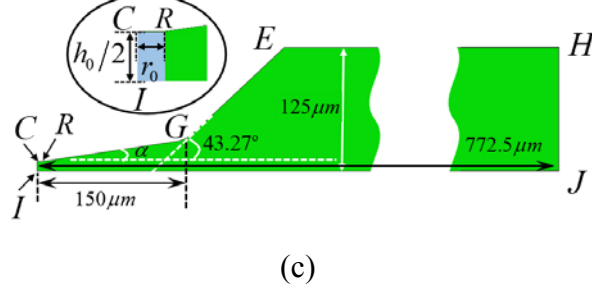

(a)   (b)

(c)
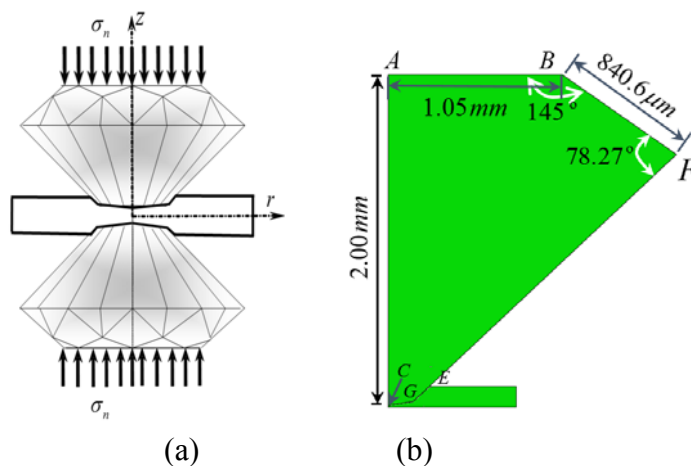
Fig. 1. Geometric parameters of the diamond anvil cell and the sample. (a) Diamond anvil cell scheme, (b) a quarter of the sample and anvil in the initial undeformed state and the geometry of anvil, and (c) the geometry of a sample and a magnified center part of a sample, which is placed in the ellipse.

Note that not only the geometry but also the boundary conditions are quite realistic. Application of the axial force Q has already been discussed. After the proper friction coefficient is chosen, the friction conditions are realistic as well; otherwise, we would not be able to reproduce the experimental pressure distribution in Fig. 2a. All other boundary conditions are trivial.

II.B. A complete system of equations for large-strain elastoplasticity for a sample

In this paper, the complete systems of equations for both the sample and the diamond anvil are summarized from [14] and [16], and computational algorithms proposed in [14] are used for the current models.

Contractions of the second-order tensors $A = \{A_{ij}\}$ and $B = \{B_{ij}\}$ over one and two indices are designated as $A \cdot B = \{A_{ij}B_{jk}\}$ and $A : B = \{A_{ij}B_{ji}\}$, respectively. The subscripts s and a designate symmetrization and anti-symmetrization, respectively, the subscripts e and p represent elastic and plastic deformation gradient or strain, the superscripts -1 and t represent the inverse and transposition of a tensor, and I is the second-order unit tensor.

Kinematics. The motion of a material with large elastic and plastic deformations is described by a vector function $r = r(r_0, t)$, where r and r_0 are the position vectors of material points in the actual configuration Ω at time instant t and in the reference configuration Ω_0 at the instant t_0, respectively. The deformation gradient

8

$$F = \frac{\partial r}{\partial r_0} = F_e \cdot F_p = R_e \cdot U_e \cdot R_p \cdot U_p = R_e \cdot U_e \cdot U_p = V_e \cdot R_e \cdot U_p, \quad \left(R_p = I; \ V_e = R_e \cdot U_e \cdot R_e^T \right) \quad (1)$$

is decomposed into elastic F_e and plastic F_p contributions, where F_p is the deformation gradient obtained after a complete release of stresses in the local vicinity of each material point, U_p and U_e are the symmetric plastic and elastic right stretch tensors, R_e and R_p are the proper orthogonal elastic and plastic rotation tensors, and V_e is the elastic left stretch tensor. The Lagrangian and Eulerian elastic strain tensors are

$$E_e = 0.5 \left(U_e \cdot U_e - I \right); \qquad B_e = 0.5 \left(V_e \cdot V_e - I \right). \qquad (2)$$

Decomposition of the velocity gradient $l = \dot{F} \cdot F^{-1} = W + d$ into the antisymmetric spin tensor $W = (l)_a$ and symmetric deformation rate $d = (l)_s$ are accepted. In combination with Eq. (1), we obtain the following decomposition of the deformation rate d into elastic and plastic contributions:

$$d = \overset{\nabla}{B_e} - 2 \left(d \cdot B_e \right)_s + V_e \cdot D_p \cdot V_e ; \quad D_p = R_e \cdot \left(\dot{U}_p \cdot U_p^{-1} \right)_s \cdot R_e^t; \quad \overset{\nabla}{B_e} = \dot{B}_e - 2 \left(W \cdot B_e \right)_s , \qquad (3)$$

where $\overset{\nabla}{B_e}$ is the Jaumann objective time derivative and D_p is the plastic deformation rate.

Elasticity rule. The following isotropic nonlinear elastic rule will be used

$$\sigma = \frac{1}{detF} (2B_e + I) \cdot \frac{\partial \Psi}{\partial B_e} , \qquad (4)$$

where $detF$ is the determinant of the tensor F, σ is Cauchy stress, and the most popular elastic potential Ψ for the extreme condition of high pressure is the third-order Murnaghan potential [27]:

$$\Psi (B_e) = \frac{\lambda_e + 2G}{2} I_1^2 - 2G I_2 + \left(\frac{l + 2m}{3} I_1^3 - 2m I_1 I_2 + n I_3 \right), \qquad (5)$$

where the second-order elastic constants are Lame constant λ_e and shear modulus G; three third-order elastic constants are l, m, and n; and I_1, I_2, and I_3 in Eq. (5) are the first, second and third invariants of the strain tensor B_e:

$$I_1 = B_{e_{11}} + B_{e_{22}} + B_{e_{33}}; \quad I_2 = B_{e_{22}}B_{e_{33}} - B_{e_{23}}^2 + B_{e_{11}}B_{e_{33}} - B_{e_{13}}^2 + B_{e_{22}}B_{e_{11}} - B_{e_{12}}^2; \quad I_3 = det\,\boldsymbol{B}_e. \qquad (6)$$

Then the Cauchy stress from Eq. (4) is

$$\boldsymbol{\sigma} = J^{-1}\left(2\boldsymbol{B}_e + \boldsymbol{I}\right) \cdot \frac{\partial \Psi\left(\boldsymbol{B}_e\right)}{\partial \boldsymbol{B}_e} = J^{-1}\left(2\boldsymbol{B}_e + \boldsymbol{I}\right) \cdot \left(\lambda_e I_1 \boldsymbol{I} + 2G\boldsymbol{B}_e + \left(lI_1^2 - 2mI_2\right)\boldsymbol{I} + n\frac{\partial I_3}{\partial \boldsymbol{B}_e} + 2mI_1\boldsymbol{B}_e\right), \quad (7)$$

where
$$\frac{\partial I_3}{\partial \boldsymbol{B}_e} = \begin{pmatrix} B_{e22}B_{e33} - B_{e23}B_{e32} & B_{e23}B_{e31} - B_{e33}B_{e21} & B_{e21}B_{e32} - B_{e22}B_{e31} \\ B_{e23}B_{e31} - B_{e33}B_{e21} & B_{e11}B_{e33} - B_{e13}B_{e31} & B_{e12}B_{e31} - B_{e11}B_{e32} \\ B_{e21}B_{e32} - B_{e22}B_{e31} & B_{e12}B_{e31} - B_{e11}B_{e32} & B_{e11}B_{e22} - B_{e12}B_{e21} \end{pmatrix}.$$

Plasticity. The pressure-dependent J_2 flow theory is used with the yield surface

$$\varphi = \sqrt{3/2\boldsymbol{s}:\boldsymbol{s}} - \sigma_y\left(p,q\right) = 0, \qquad (8)$$

where $\boldsymbol{s}$ is the deviatoric Cauchy stress and σ_y is the yield strength, which depends on the mean pressure p and the accumulated plastic strain q defined as

$$\dot{q} = \left(2\boldsymbol{D}_p : \boldsymbol{D}_p/3\right)^{0.5}. \qquad (9)$$

The plastic flow rule is presented as

$$\boldsymbol{D}_p = \lambda \,\boldsymbol{s}\Big/\sqrt{\boldsymbol{s}:\boldsymbol{s}}, \qquad (10)$$

where $\lambda\,(\lambda > 0)$ is a scalar function determined from the consistency condition $\dot{\varphi} = 0$.

The traditional equilibrium equations in the current configuration are used

$$\nabla \cdot \boldsymbol{\sigma} = \boldsymbol{0}. \qquad (11)$$

It was found in [28] that for more than 60 materials belonging to different classes (*e.g.* metals, rocks, alloys, oxides, compacted powders), above some level of plastic strain and for a deformation path without sharp changes in direction (monotonous deformation), the initially-isotropic polycrystalline materials are deformed as a perfectly plastic and isotropic material with a strain history-independent limiting surface of the perfect plasticity. This means that, above some critical q, the accumulated plastic strain q is excluded from the relationship for the yield

LA-UR-18-23227

strength in Eq. (8), i.e. $\sigma_y(p,q)=\sigma_y(p)$. We assume that the critical strain is reached in all points of the sample during its preparation (pre-indentation), and we will use the perfectly plastic (i.e. plastic strain-independent) model. This significantly simplifies the model and its calibration while still allowing us to describe experiments for rhenium. The linear dependence of yield strength on pressure p is accepted in this paper

$$\sigma_y(p)=\sigma_{y0}+bp, \tag{12}$$

where σ_{y0} is the yield strength at the pressure $p=0$ and b is a parameter.

Material parameters. Rhenium has been of particular interest due to its large bulk (K) and shear (G) moduli and high strength [4, 29], and it is widely used as the sample and gasket material in a DAC [1-4]. The following properties of rhenium are used in simulations: Elastic constants [4, 14, 29] in Eqs. (5) and (7): $G=200\,\text{GPa}$, $\lambda_e=247\,\text{GPa}$, $l=-291\,\text{GPa}$, $m=-662$ GPa and $n=0$, and plastic constants [4, 14] $\sigma_{y0}=8.00\,\text{GPa}$ and $b=0.04$.

II.C. Nonlinear anisotropic elasticity for single-crystal diamond

The traditional elasticity rule has the form

$$\boldsymbol{\sigma}=\boldsymbol{F}\cdot\tilde{\boldsymbol{T}}(\boldsymbol{E})\cdot\boldsymbol{F}^t\big/\det\boldsymbol{F}; \qquad \boldsymbol{T}=\boldsymbol{\sigma}\det\boldsymbol{F}=\boldsymbol{F}\cdot\tilde{\boldsymbol{T}}(\boldsymbol{E})\cdot\boldsymbol{F}^t; \qquad \tilde{\boldsymbol{T}}=\partial\Psi\big/\partial\boldsymbol{E}, \tag{13}$$

where $\boldsymbol{T}$ is the Kirchhoff stress and $\tilde{\boldsymbol{T}}$ is the second Piola-Kirchhoff stress. Because there is no plastic deformation in a diamond, the subscript e is dropped. Under megabar pressures, it is necessary to consider at least the third-order potential Ψ with the cubic symmetry:

$$\Psi=0.5c_{11}\left(\eta_1^2+\eta_2^2+\eta_3^2\right)+c_{12}\left(\eta_1\eta_2+\eta_1\eta_3+\eta_2\eta_3\right)+0.5c_{44}\left(\eta_4^2+\eta_5^2+\eta_6^2\right)+c_{111}\left(\eta_1^3+\eta_2^3+\eta_3^3\right)/6$$
$$+0.5c_{112}\left[\eta_1^2\left(\eta_2+\eta_3\right)+\eta_2^2\left(\eta_1+\eta_3\right)+\eta_3^2\left(\eta_1+\eta_2\right)\right]+c_{123}\eta_1\eta_2\eta_3+0.5c_{144}\left(\eta_1\eta_4^2+\eta_2\eta_5^2+\eta_3\eta_6^2\right) \tag{14}$$
$$+0.5c_{166}\left[\left(\eta_2+\eta_3\right)\eta_4^2+\left(\eta_1+\eta_3\right)\eta_5^2+\left(\eta_1+\eta_2\right)\eta_6^2\right]+c_{456}\eta_4\eta_5\eta_6,$$

where $\eta_1=E_{11}$, $\eta_2=E_{22}$, $\eta_3=E_{33}$, $\eta_4=2E_{23}$, $\eta_5=2E_{31}$, and $\eta_6=2E_{12}$.

11

Then the second Piola-Kirchhoff stress $\tilde{T}$ or Cauchy stress σ can be directly obtained, based on Eqs. (13) and (14). Two explicit examples for the components of $\tilde{T}$ are given below:

$$\tilde{T}_{11} = \partial\Psi\big/\partial\eta_1 = c_{11}\eta_1 + c_{12}(\eta_2 + \eta_3) + c_{111}\eta_1^2/2 + c_{112}\left[2\eta_1(\eta_2+\eta_3) + \eta_2^2 + \eta_3^2\right]/2 + c_{123}\eta_2\eta_3$$

$$+c_{144}\eta_4^2/2 + c_{166}(\eta_5^2 + \eta_6^2)/2; \quad \tilde{T}_{12} = \partial\Psi\big/\partial\eta_6 = c_{44}\eta_6 + c_{144}\eta_3\eta_6 + c_{166}(\eta_1 + \eta_2)\eta_6 + c_{456}\eta_4\eta_5. \tag{15}$$

In this paper, the second-order elastic constants are [30]: $c_{11} = 1050\,\text{GPa}$, $c_{12} = 127\,\text{GPa}$, and

$c_{44} = 550\,\text{GPa}$, and the third-order elastic constants are [26]: $c_{111} = -7603\text{GPa}$, $c_{112} = -1909\text{GPa}$,

$c_{123} = -835\text{GPa}$, $c_{166} = -3938\text{GPa}$, $c_{144} = 1438\text{GPa}$, and $c_{456} = -2316\text{GPa}$.

In simulations, the friction coefficient in the Coulomb friction rule is $\mu = 0.1$.

III.   RESULTS AND DISCUSSION IN THE SAMPLE UNDER EXTREME PRESSURES

III.A. Overview

Our results [14] reproduced the pressure distribution in experiments [3] up to 300 GPa. Cupping was observed experimentally [3] under pressure near 300 GPa, but does not appear in our simulations [14] when we use the third-order elastic constants from [26]. It will be found that this is because a very short, flat contact surface (the line *CR* in Fig. 1c) used in experiments was ignored in previous FEM simulations [14]. At the beginning of this section, we will use the flat part $r_0 = 5\,\mu\text{m}$ and the beveled angle $\alpha = 8.5^\circ$, which are taken from experiments [3]. The sample is assumed to be pre-indented into the initial thickness as $h_0 = 20\,\mu\text{m}$ at the center (*r*=0), which is commonly used in experiments (see [1]). This set of geometric parameters ($r_0 = 5\,\mu\text{m}$, $\alpha = 8.5^\circ$, and $h_0 = 20\,\mu\text{m}$) are used for results in Figs. 2-4. To study the effects of the radius of

12

the flat part r_0 in Figs. 5 and 6, we vary r_0 from 0 to 5 and 10 μm, with the fixed $\alpha = 8.5^\circ$ and

$h_0 = 20\,\mu m$. The effects of the beveled angle in Fig. 7 are studied by comparing the results with

$\alpha = 7.5^\circ$ and 9.5° for $r_0 = 10\,\mu m$ and $h_0 = 20\,\mu m$. Fig. 8 shows the effects of the initial

thickness of the sample by comparing results for $h_0 = 20$ and $40\,\mu m$, with $\alpha = 8.5^\circ$ and

$r_0 = 0\,\mu m$. The effect of the sample strength will be studied by comparing the results of

$\sigma_{y0} = 8.00\,GPa$ and $\sigma_{y0} = 4.00\,GPa$ with the same gasket properties and geometrical parameters:

$h_0 = 10\,\mu m$ with $\alpha = 9.5^\circ$ and $r_0 = 10\,\mu m$.

III.B. Stresses and plastic flow for $r_0 = 5\,\mu m$, $\alpha = 8.5^\circ$ and $h_0 = 20\,\mu m$

Fig. 2 plots the distributions of pressure and shear stress under an increasing applied stress σ_n.

Our simulation results in curve 4 coinciding with experimental data in [3]. The major difference

between the current and previous simulation results [15] is that the pressure gradient in this paper

is much larger at the center of the sample but smaller at the periphery than that in [15].

The distribution of shear stresses (friction stress) τ_f in Fig. 2b coincides with the distribution of

the pressure-dependent yield strength in shear $\tau_y(p)$ for most of the contact region with a low

load (see curve 1 and 2). This means that the plastic friction condition $\tau_f = \tau_y(p)$ is fulfilled in

this region. While it is not included explicitly in the contact sliding condition, this indicates the

occurrence of localized plastic flow in a thin contact layer, which is equivalent to the contact

sliding. With an increase of compressive loads from curve 3 to curve 5, the shear stress

decreases at the center of the sample, and there is an increasing region where the friction stress

τ_f is smaller than $\tau_y(p)$. This is caused by changing the direction of the material flow as shown

13

in Fig. 3. The variation of the maximum pressure in the sample versus the applied compressive force or the normal applied stress σ_n is plotted in Fig. 2c. This curve in Fig. 2c qualitatively reproduces all three stages of corresponding experimental curve in Ref. 9. Initial linear dependence up to 1.5 kN (15 GPa) corresponds to low contact friction and relatively large sample thickness. In the range from 1.5 to 6 kN (160 GPa), friction stress reaches the yield strength in shear and, due to significant reduction in the sample thickness, growth in pressure gradient and maximum pressure accelerates. After the deflection point, pressure growth decelerates (a) due to slower reduction in thickness, (b) reduction of the contact friction stress relative to the yield strength in shear, and (c) the bending and cupping of anvils, partial plastic flow to the center, and transition from plastic to elastic deformations of the central part of a sample. Based on the trend in Fig. 2c, it is clear that further increase in pressure will require significant increase of the applied force, which will lead to fracture of an anvil.

In [14], even without the flat part CR ($r_0 = 0$), the pressure distribution was also consistent with experiments, but the cupping at the pressure near 300 GPa was not reproduced. With a short, flat part, case 5 in Fig. 3 clearly shows that the cupping appears at σ_n =3.011 GPa, where the maximum pressure is 300 GPa at the center in Fig. 2a. Here, we should mention that cupping can cause a sudden drop of pressure distribution at the periphery, as is shown in curve 5 at $r = 140\,\mu m$. Similar pressure drops due to cupping can be found in this paper for all other cases with different geometric parameters. More importantly, a similar cupping-related pressure drop has been observed experimentally [9].
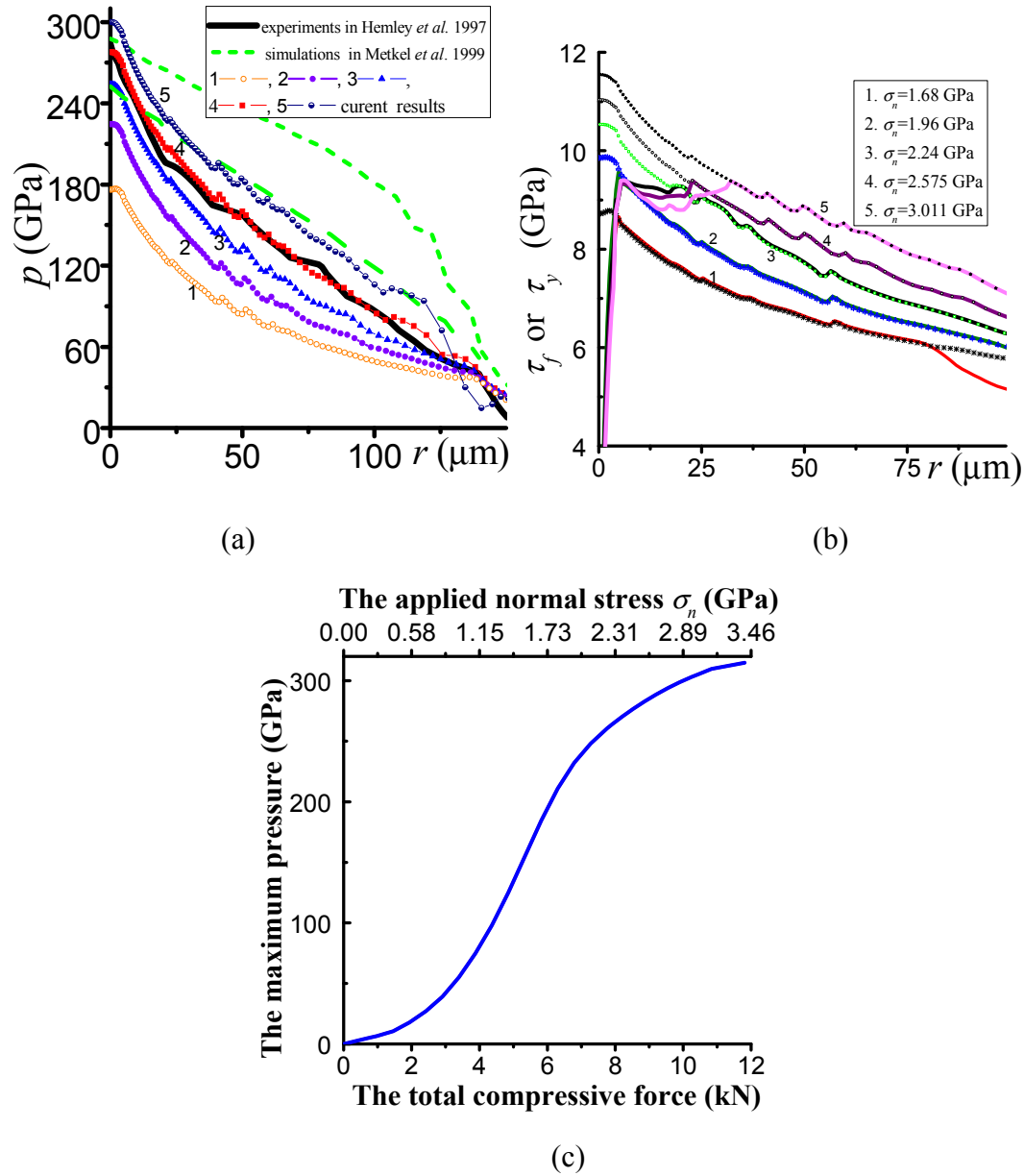
LA-UR-18-23227

Fig. 2. Distributions of pressure p (a), friction stress τ_f (solid lines), and yield strength in shear τ_y (doted lines) (b) at the contact surface of a sample for $r_0 = 5\mu m$ under an increasing applied normal stress σ_n: 1.68 GPa (1), 1.96 GPa (2), 2.24 GPa (3), 2.575 GPa (4), and 3.011 GPa (5). In (a), dotted curves 1-5 are the current simulation results, the two green dashed curves are the simulation results from [13], and the solid black curve represents the experimental results from [3]. (c) Maximum pressure in the sample versus the applied force or normal stress.

15

Important information can be learned from Figs. 3 and 4, which present the velocity along the radial direction v_r and the rate of accumulated plastic strain $\dot{q}$. Because time is not a parameter for the current rate-independent plasticity and static problem formulation, the magnitudes of $\dot{q}$ and v_r can be made arbitrary by changing the rate of loading. This does not change the stress and strain distribution at each load, independent of how fast it is achieved. The results in Figs. 3 and 4 are presented for constant $\dot{\sigma}_n = 0.7 \times 10^{-4} \, \text{GPa·s}^{-1}$. Consequently, only the relative values in the distributions of $\dot{q}$ and v_r for any state (or load σ_n) are important. The radial velocity in the diamond anvils is always negative (i.e. directed toward the center), except at the central line $z=0$ where the velocity is zero, and its magnitude increases with a rising radial coordinate. It is found from Fig. 3 that initially, at $\sigma_n = 1.68 \, \text{GPa}$, the whole sample flows "fast" from the center to the periphery. With an increase in the applied force σ_n, starting from the center of the sample, the radial velocity v_r changes direction and materials "slowly" move from the periphery to the center. For $\sigma_n = 3.011 \, \text{GPa}$, material motion towards the center is observed in the major region of a sample.

It may seem counterintuitive that material velocity changes sign within a sample but contact shear stresses in Fig. 2b do not. The negative velocity v_r and its gradient along the thickness direction are very small (by one order of magnitude) in comparison with the material flows from the center to the periphery at the external part of a sample. Because plastic flow is incompressible, deformation in this region is either elastic or with small plastic strains. This is in agreement with small values of $\dot{q}$ in this region (Fig. 4). The key point is that, due to deformation of diamond, relative sliding velocity at the contact surface is either zero or positive. This is why the sign of the contact shear stress does not change.
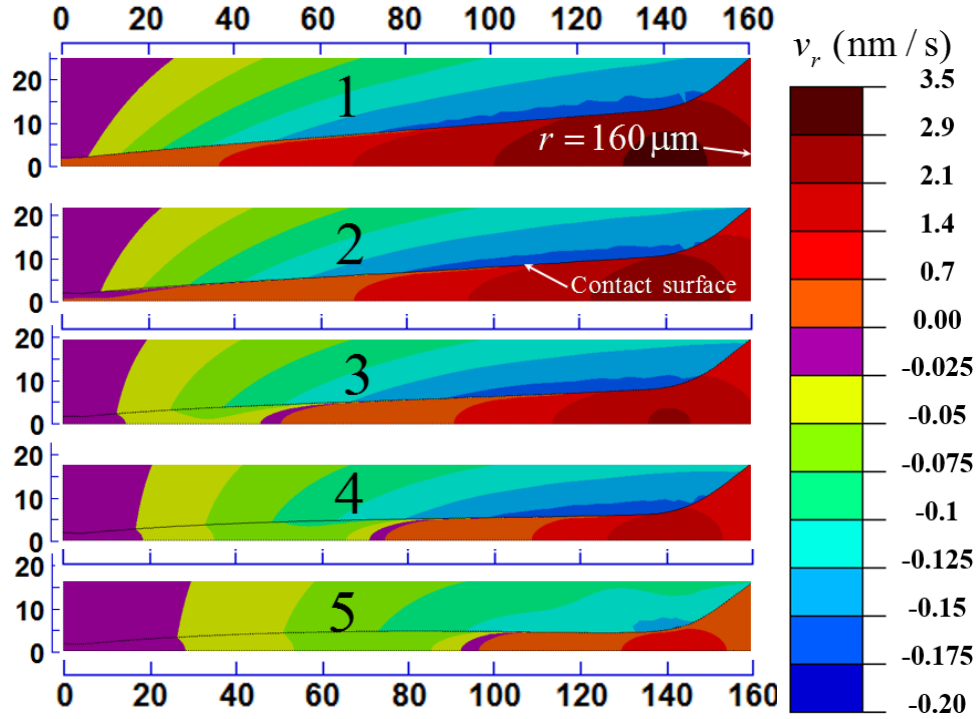
Fig. 3. Distribution of radial velocity v_r in the sample and diamond $(0 \leq r \leq 160\,\mu\text{m})$ with $r_0 = 5\,\mu\text{m}$ under an increasing applied normal stress σ_n. The normal stress σ_n is 1.68 GPa (1), 1.96 GPa (2), 2.24 GPa (3), 2.575 GPa (4), and 3.011 GPa (5).

Fig. 4 shows the distribution of the rate of accumulated plastic strain $\dot{q}$. Initially, at σ_n =1.68 GPa, the entire region is under plastic straining. The accumulated plastic strain rate shows the shear band near the contact surface, where shear stresses reach the yield strength in shear. Excluding this region, $\dot{q}$ is not very heterogeneous along the radius because the radial velocity increases with r while the sample thickness increases as well. As the applied stress σ_n increases from 1.96 GPa to 2.24 GPa, $\dot{q}$ is nonzero but quite small in the region with negative velocity v_r in Fig. 3. With the further increase of applied stresses, the rate of accumulated plastic strain significantly decreases and the location with the maximum rate of the accumulated plastic strain moves towards the periphery. At σ_n =2.575 GPa, $\dot{q}$ becomes zero at the center of a sample,

17

demonstrating an unusual transition from plastic to the elastic state under an increased load. The region without plastic deformation grows, and $\dot{q}$ decreases in the rest of the sample as σ_n increases. One reason for this is that the bending of the anvil reduces the speed of the thickness reduction rate. As a result, the pressure and pressure gradient cannot continuously increase when cupping becomes significant (see also the experiment in Ref. 3); this can be explained by a simplified equilibrium equation (see e.g. [16, 28, 31])

$$\frac{dp}{dr} = -\frac{2\tau_f}{h}.\qquad(16)$$

Indeed, the thickness h cannot be reduced further after some critical value. The final (minimum) sample thickness in Fig. 4 under $\sigma_n = 3.011$ GPa is $3.38\,\mu m$, which is consistent with the experimental value of approximately $3\,\mu m$ in [3].
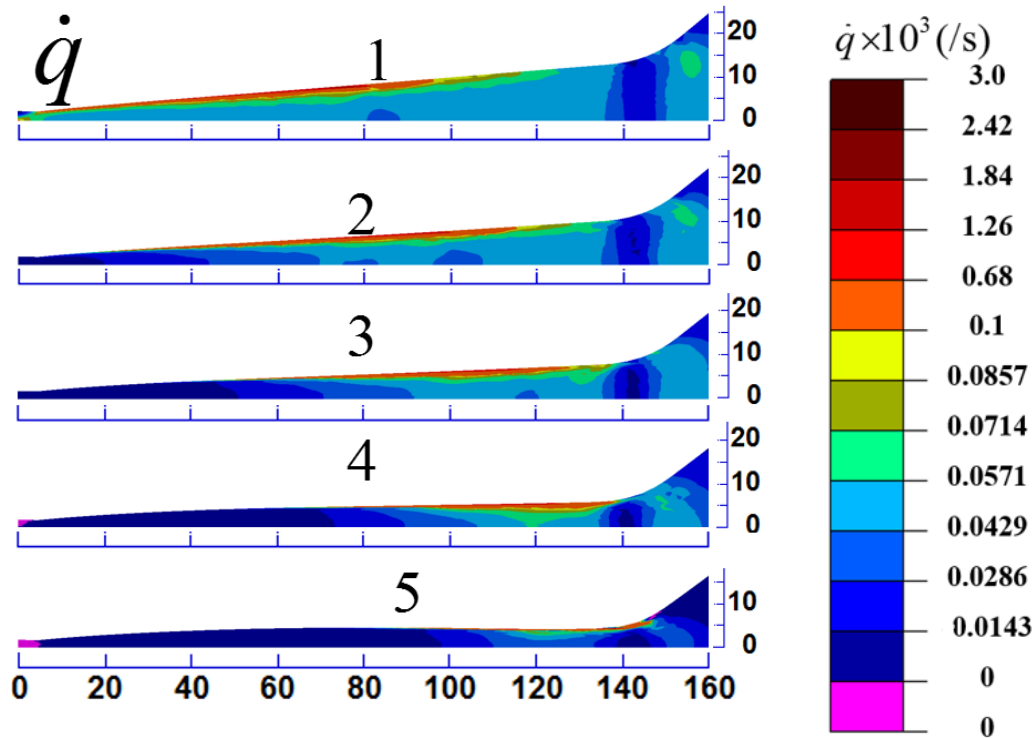

Fig. 4. Distributions of the rate of accumulated plastic strain $\dot{q}$ in the sample $(0 \le r \le 160\,\mu m)$ with $r_0 = 5\,\mu m$ under an increasing applied normal stress σ_n. The normal stress σ_n is

18

1.68 GPa (1), 1.96 GPa (2), 2.24 GPa (3), 2.575 GPa (4), and 3.011 GPa (5). In the magenta region, the plastic strain rate is exactly zero.

III.C. Effect of the radius of the flat diamond tip

Fig. 5 plots the distributions of pressure and the z coordinate of the contact surface for radii of the flat diamond tip r_0 that vary from 0 to 5 to 10 μm when *the maximum pressure reaches 293 GPa*. Note that, in experiments, the axial force (equivalent to the normal stress σ_n) is applied. Thus, comparison at the same maximum pressure requires the application of different σ_n (Fig. 5). A shorter flat part *CR* indicates a longer inclined part *RG* in Fig. 1c, as the radial distance *CG* is fixed at 150 μm. At a given applied stress σ_n but with different r_0, the shorter the flat diamond tip radius r_0 is, the faster the plastic flow along the radial direction and the thickness reduction are. This is because the inclined diamond surface with a positive slope instead of the flat diamond tip favors the material flows to the periphery. The faster thickness reduction causes a larger pressure and pressure gradient at the center due to the simplified equilibrium condition (16) and indicates that, for the same maximum pressure at the center, the applied normal stress σ_n is an increasing function of the radius of the flat part r_0 (Fig. 5). Fig. 5b plots the z coordinate of the contact surface (equal to half a thickness of sample $h/2$) for $r_0 = 0$, 5 and 10 μm. The smaller r_0 and, consequently, σ_n lead to faster thickness reduction at the center, but smaller deformation of an anvil both at the center and at the periphery. Cupping near the sample center appears for any initially flat surface and increases with increasing r_0. At the periphery, cupping does not appear with $r_0 = 0$; it only appears for $r_0 = 5$, and it becomes very obvious for 10 μm.

19

Similar to Fig. 2a, the cupping causes the pressure drop at the periphery for r_0 =10 μm in Fig. 5a, like in experiment [9]. Thus, for *the same maximum pressure*, an increase in the diamond tip radius essentially increases the pressure everywhere except at the center, increases the total force, and increases the bending of an anvil at both the center and the periphery.
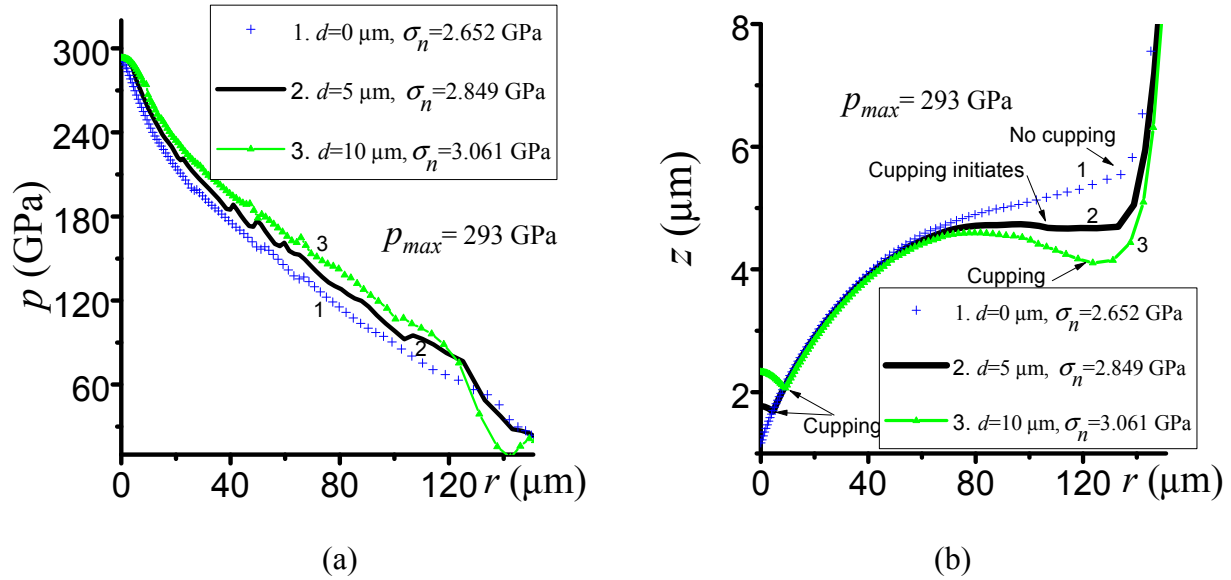

Fig. 5. Distributions of the pressure p at the sample contact surface (a) and the z coordinate of diamond/sample contact surface (b) when the maximum pressure is p= 293 GPa at r=0 at the contact surface. The applied stress σ_n is 2.652 GPa (1), 2.849 GPa (2), and 3.061 GPa (3). Cupping and double cupping formation is shown.

Very different conclusions can be made if one compares the effect of the diamond tip radius r_0 at 0 and 10 μm on the distribution of pressure and the profile of contact surface at *the same applied load* (Fig. 6). *Under the same applied load, the pressure distribution and thickness of the sample are the same everywhere except at the center of the sample.* For r_0 =0, material flows much faster at the center than for r_0 =10 μm in Fig. 6b, which causes a larger pressure gradient and pressure at the center of sample. With the increasing applied load σ_n, the difference in pressure at the center for both cases becomes more obvious. At σ_n =1.681 GPa, the difference in

20

pressure is only 6 GPa; at σ_n=3.061 GPa, the difference in pressure becomes 21 GPa. This is because as the thickness reduces, the difference in $1/h$ increases and the pressure gradient linearly depends on $1/h$. For example, the ratios of $1/h$ at r=0 between r_0=0 and 10 μm are 1.8 with σ_n=1.681 GPa and 2.03 with σ_n=3.013 GPa.
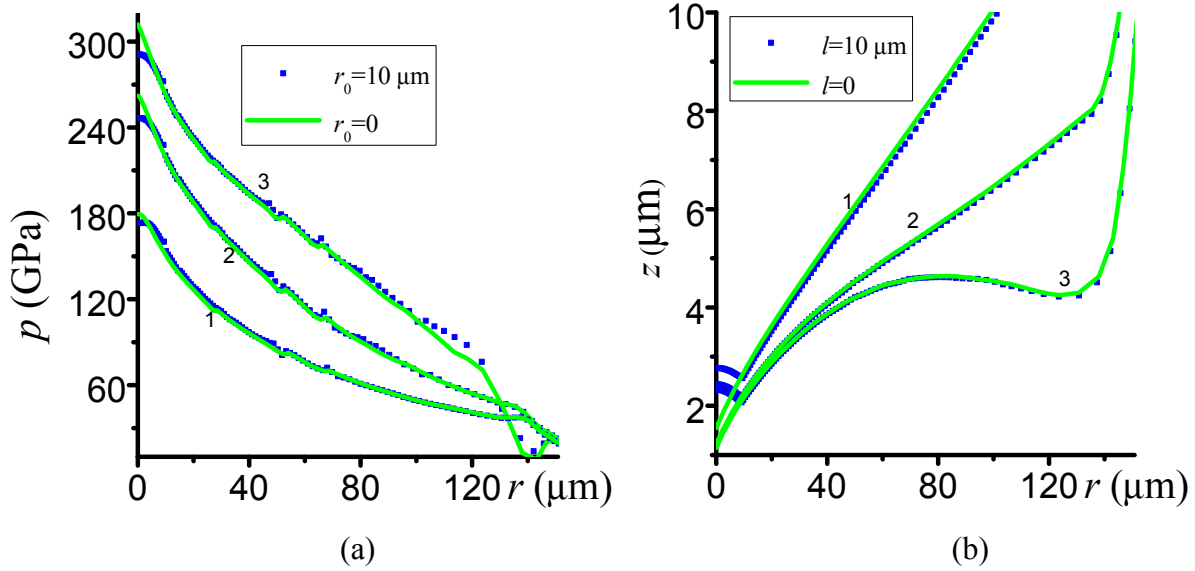

Fig. 6. Distributions of pressure p at the contact surface of a sample and z coordinate of the diamond/sample contact surface for $r_0 = 0$ and $10\,\mu$m under three values of applied stress σ_n: 1.681 GPa (1), 2.241 GPa (2) and 3.013 GPa (3).

Comparing curves 2 and 3 in Fig. 6b, one concludes that, for a maximum pressure above 250 GPa, the increase in force fails to reduce the thickness of a sample for the beveled surface for both $r_0 = 0$ and $10\,\mu$m and results in bending at the periphery of the sample. Cupping at the center does not occur for $r_0 = 0$ and occurs at any force under study for $r_0 = 10\,\mu$m.
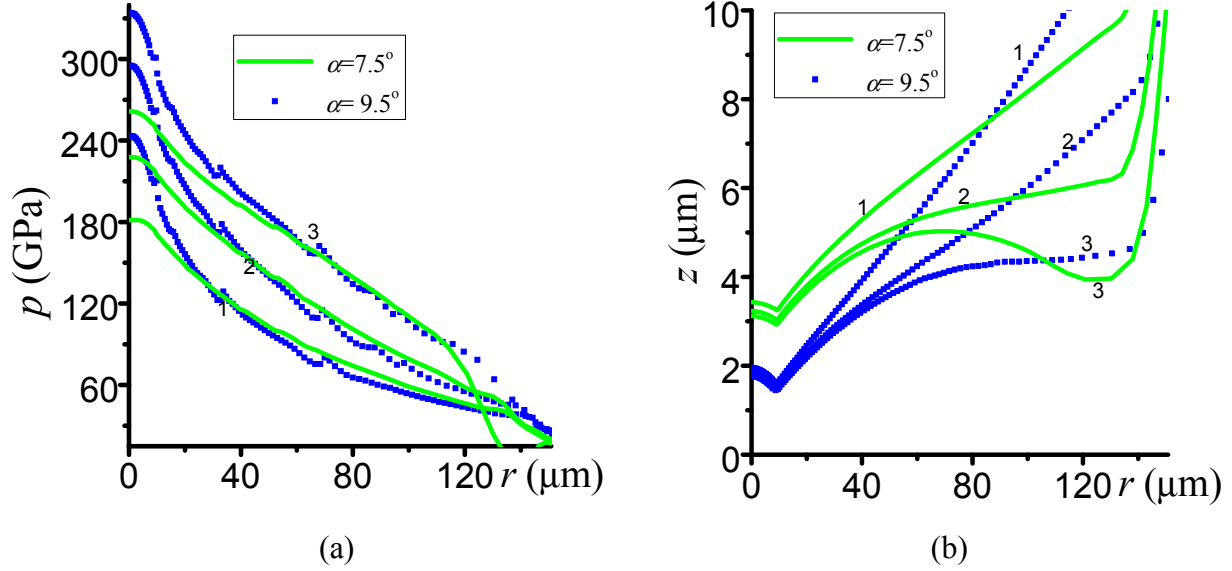
III.D. Effect of the bevel angle

Fig. 7. Distributions of pressure p at the contact surface of the sample (a) and z coordinate of diamond/sample contact surface (b) for $r_0 = 10\,\mu m$ and two bevel angles, $\alpha = 7.5°$ or $9.5°$, under three applied normal stresses σ_n: 1.868 GPa (1), 2.365 GPa (2), 3.045 GPa (3).

The effect of the bevel angle α is shown in Fig. 7. With a larger beveled angle $\alpha = 9.5°$, the material flow from the center to the periphery is more intense, causing a much faster thickness reduction at the center than for $\alpha = 7.5°$. Smaller thickness of a sample at the center for $\alpha = 9.5°$ causes a larger pressure gradient and pressure at the center than for $\alpha = 7.5°$. In addition, for an larger bevel angle, cupping at the periphery is postponed: at $\sigma_n = 3.045$ GPa, the cupping is obvious for $\alpha = 7.5°$ and does not exist for $\alpha = 9.5°$. In addition, cupping at the center is slightly larger for $\alpha = 9.5°$. We note that, at the periphery, the thickness is smaller for $\alpha = 7.5°$ than for $\alpha = 9.5°$ due to the smaller initial thickness and larger diamond bending and cupping. At the periphery, the thickness reduction rate is also faster with a larger bevel angle. For example, the differences of the z coordinate at $r = 120\,\mu m$ between cases with $\alpha = 9.5°$ and $7.5°$ are 1.3 μm, 1.0 μm, and 0.5 μm for the applied loads σ_n of 1.4 GPa, 1.75 GPa and 2.652 GPa, respectively.

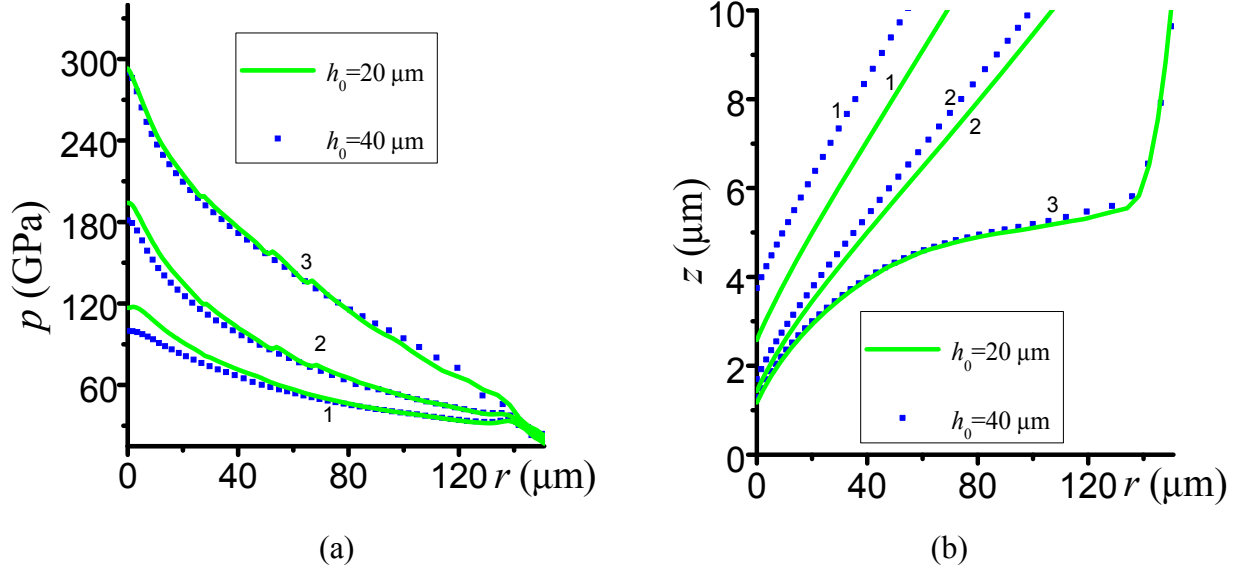### III.E. Effect of initial sample thickness

22

Fig. 8. Distributions of pressure p at the contact surface of a sample (a) and z coordinate of the diamond/sample contact surface (b) for $r_0 = 0\,\mu\text{m}$ and initial thicknesses of $h_0 = 20\,\mu\text{m}$ or $40\,\mu\text{m}$ at the center of the sample under applied normal stress σ_n: 1.4 GPa (1), 1.75 GPa (2), 2.652 GPa (3).

In Figs. 2-7, the sample is pre-indented to the initial thickness of 20 μm at the center. In Fig. 8, we compare results for $h_0 = 20\,\mu\text{m}$ with those for $h_0 = 40\,\mu\text{m}$. Under a small applied normal stress σ_n=1.4 GPa, Fig. 8b shows that material flows to the periphery much faster with a larger initial thickness $h_0 = 40\,\mu\text{m}$, because the difference of z coordinate at the center is initially 10 μm and is only 1.2 μm under σ_n=1.4 GPa. Due to a smaller thickness in the deformed configuration, the pressure at the center with the initial thickness with $h_0 = 20\,\mu\text{m}$ is 17 GPa larger than the pressure with $h_0 = 40\,\mu\text{m}$. With the increase of the r coordinate, the difference in pressure distribution decreases while the difference in h undergoes practically no change. It is noted that the differences caused by the initial thickness significantly decrease with an increase of applied normal stress. At σ_n=2.652 GPa, the distributions of both the pressure and thickness of the sample are almost the same for $h_0 = 20\,\mu\text{m}$ and $40\,\mu\text{m}$.

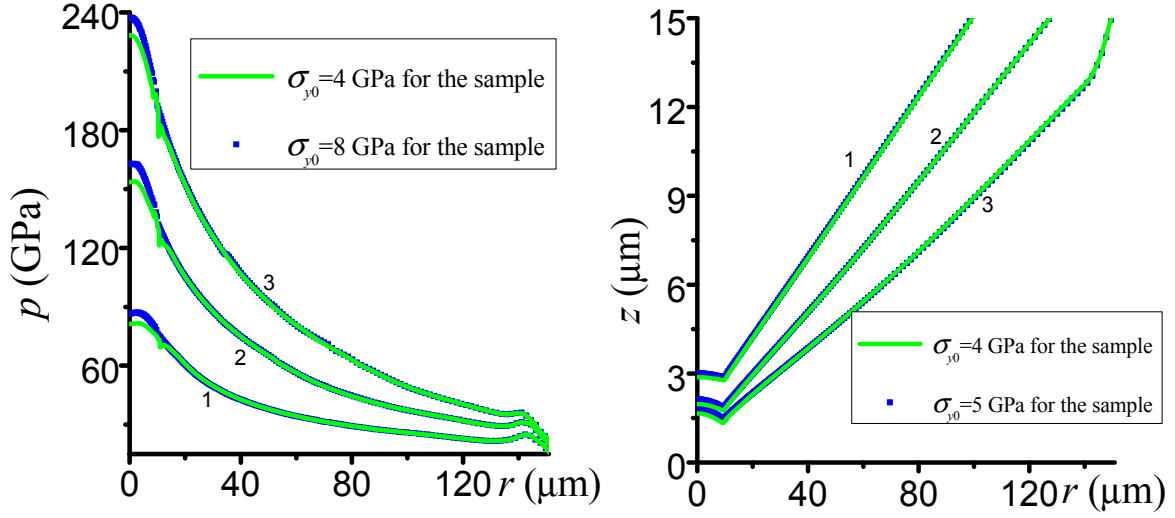**III.F. Sample-gasket system: effect of the sample strength**

23

Fig. 9. Distributions of pressure p at the contact surface of a sample (a) and z coordinate of the diamond/sample contact surface (b) for $\alpha = 9.5°$, $r_0 = 10\,\mu m$, and the initial sample thickness $h_0 = 10\,\mu m$ under the applied normal stress σ_n: 1.05 GPa (1), 1.4 GPa (2), 1.75 GPa (3). For the green solid line: the cylindrical sample of the radius $10\,\mu m$ has the same material properties as the rhenium gasket (for $r > 10\,\mu m$) except for $\sigma_{y0} = 4.0$ GPa, keeping $\sigma_{y0} = 8.0$ GPa for the gasket; for the blue symbol line, the entire region (gasket and sample) is rhenium. Coulomb friction is used for all contact surfaces.

Let us consider a sample material in the cylinder of radius $10\,\mu m$, which is the same as the radius of the flat part (see the blue part of the magnified area in Fig. 1c). It has the same properties as the rhenium gasket, but with $\sigma_{y0} = 4.0$ GPa instead of $\sigma_{y0} = 8.0$ GPa for the gasket. The results are shown in Fig. 9. With a softer sample, the pressure gradient and, consequently, the pressure are expected to be smaller at the center of a sample because the friction stress $\tau_f \le \tau_y$ is smaller in the equilibrium equation (16). The thickness of a softer sample is slightly smaller in Fig. 9b, which slightly increases the pressure gradient. However, the effect of a weaker friction stress dominates, causing a lower pressure gradient and pressure in a

24

weaker sample (Fig. 9a). However, the reduction is relatively small for such a small sample because, close to the center for any σ_{y0}, the friction stress decreases to zero at the symmetry axis. The change in pressure distribution in the gasket is negligible because small changes in stresses over a small sample area at fixed total force have a negligible effect on the force over the large gasket area.

Note that in experiments, micro-semi balls made of nanodiamond have been placed at the center, allowing extreme pressures of 600 GPa [1] and 750 GPa [2] to be reached. This pressure increase is easily rationalized by a decrease in the sample thickness in the simplified equilibrium equation.

IV. CONCLUDING REMARKS

In this paper, FEM simulations are conducted to investigate large elastoplastic deformations of rhenium and elastic deformation of diamond under pressures up to 300 GPa in DAC, with an emphasis on the effects of geometric and material properties. A thermodynamically-consistent isotropic model for large elastic and plastic deformations of a compressed material with pressure-dependent yield strength and a nonlinear anisotropic model for diamond, developed in [14, 24], were used.

In the paper, the following experimental phenomena have been reproduced:

(1) the pressure distribution at the sample/diamond contact surface at pressure up to 300 GPa in [3];

(2) the final sample thickness around 3 μm in experiment [3] at the pressure of 300 GPa;

(3) the cupping phenomenon taking place at the pressure 300 GPa [3];

(4) the double cupping phenomenon at megabar pressures in [9];

25

(5) three stages at the curve of the maximum pressure versus compressive force in [9];

(6) stages of material flow with increasing load obtained in experiments [3,9];

(7) pressure drop at the periphery after cupping in that region [9], and

(8) change in the direction of material flow to the center without change in the sign of the pressure gradient in [3,9]. Note that, in contrast to our previous study [14], these confirmations have been obtained while utilizing the third-order elastic constants of diamonds from [26] without any artificial corrections.

While our model is calibrated and shows good correspondence with experiments in [3] up to 300 GPa, it includes all of the necessary components (finite elastic and plastic deformations, pressure dependence of the yield strength, and nonlinear elasticity) to be applicable in principle for much higher pressure. However, comparison with experiments for much higher pressure may necessitate the introduction of more complex constitutive equations, particularly even higher-order elasticity for rhenium and diamond and nonlinear pressure dependence of the yield strength. Therefore, the maximum pressure did not exceed 340 GPa (Fig. 7 (a)) in our simulations.

Cupping at the center and/or periphery of the anvil is the main phenomenon at the megabar pressures that produces counterintuitive phenomena and limits the maximum pressure. Cupping is caused by large bending-type deformation of a diamond anvil and causes the transition from the material plastic flow from the center to the periphery to partial flow to the center, followed by elastic deformation without or with small plasticity, all under an increasing force. These processes are described and studied in detail in the paper. In particular, elastic rather than plastic deformation of the sample requires a significant increase in force to produce further reduction in the sample thickness and maximum pressure. Such an overloading of an anvil finally leads to its plastic deformations and fracture, which are not considered here. The modern

experimental way to overcome this limitation is to utilize a two-stage loading system, placing micro-semi balls made of nanodiamond at the center of the anvil's tips [1,2]. A paradoxical result, for which the material flow to the sample center does not change the sign of the contact shear stress and pressure gradient, is found. This is explained by finding that, due to deformation of the diamond, relative contact sliding does not change sign or is absent. The distribution of the contact shear stresses coincides with the distribution of the pressure-dependent yield strength in shear, excluding regions near the center of a sample and, for the lowest load, at the periphery. This means that plastic friction is realized by localized plastic flow below the contact surface.

We would like to stress that comparison of the effect of different parameters on the DAC mechanical behavior may strongly depend on whether the comparison is performed under the same applied load or maximum pressure at the center. For example, under the same applied load, an increase in the radius of the flat diamond tip reduces pressure and increases the sample thickness under the tip, but does not affect them at the beveled surface until cupping appears. However, at the same maximum pressure at the center, the increase in the flat tip radius increases pressure everywhere except at the very center, increases the total force, and increases the bending of an anvil at both the center and the periphery. As mentioned, introducing the flat tip allows us to reproduce cupping at the periphery, which is absent at the same maximum pressure without the flat diamond tip.

At the same applied force, a small increase in the bevel angle increases the pressure gradient and pressure at the center, as well as cupping at the center, but reduces cupping at the periphery. Increasing the sample thickness reduces the pressure gradient and pressure at the initial compression stages. This effect decreases with increasing compression and disappears at

large compression. A small, weaker sample within the gasket slightly reduces the pressure in a sample and does not affect the gasket.

The obtained results improve the understanding of strongly-nonlinear mechanical responses of the DAC under extreme pressures and large elastoplastic deformations. In the future, they may be utilized as a tool for computational optimum design of DAC. Review of some computational works on the optimization of the anvil's geometry and loading conditions is presented in [14]. However, optimization was based on consideration of only an anvil within linear elasticity, which is applicable at relatively low pressure. The main work that must be done before numerical optimization is possible at the megabar pressure is the development of plastic flow and fracture criteria for the diamond at the megabar pressures. Since high pressures can be obtained under very heterogeneous stress states only, it is impossible to find these criteria from an experiment without corresponding modeling. This should include:

(a) the first principle simulations of stress-strain curves and all lattice instabilities which can lead to dislocation and crack nucleation under various complex loadings;

(b) development of continuum models that include dislocation and crack nucleation and evolution, which are calibrated by atomistic simulations; and

(c) implementing these models for diamond in simulations similar to those presented in the current work, performing simulations and checking fracture conditions against experiments.

In the case of success, these models can be used for computational optimum design of DAC. There are two main goals: (a) to reach record high pressure once or multiple times and (b) to reach the required high pressure in the largest possible sample once or multiple times. As the next step, we will use some of the recent experimental results up to 400 GPa in [9] for tungsten

to calibrate our model and then reproduce all of the experimental results in [9]. Phase transformations in a sample will also be included, similar to what we did in [32] for boron nitride, where a lower pressure range was considered. Some other directions in a coupled modeling and experimental studies of the mechanical and transformation processes under high pressure are outlined in [33].

Acknowledgements

References

[1]   L. Dubrovinsky, et al., The most incompressible metal osmium at static pressures above 750 gigapascals, Nature **525**, 226 (2015).

[2]   L. Dubrovinsky, N. Dubrovinskaia, V. B. Prakapenka, and A. M. Abakumov, Implementation of micro-ball nanodiamond anvils for high-pressure studies above 6 Mbar, Nat. Commun. **3** (2012).

[3]   R. J. Hemley, H. K. Mao, G. Y. Shen, J. Badro, P. Gillet, M. Hanfland, and D. Hausermann, X-ray imaging of stress and strain of diamond, iron, and tungsten at megabar pressures, Science **276**, 1242 (1997).

[4]   R. Jeanloz, B. K. Godwal, and C. Meade, Static strength and equation of state of rhenium at ultra-high pressures, Nature **349**, 687 (1991).

[5]   H. K. Mao and P. M. Bell, High-pressure physics: sustained static generation of 1.36 to 1.72 megabars, Science **200**, 1145 (1978).

[6]   R. P. Dias, I. F. Silvera, Observation of the Wigner-Huntington transition to metallic hydrogen, Science **355**, 715–718 (2017).

[7]   X.-D. Liu, P. Dalladay-Simpson, R. T. Howie, B. Li, E. Gregoryanz, Comment on "Observation of the Wigner-Huntington transition to metallic hydrogen", Science **357**, eaan2286 (2017).

[8]   I. F. Silvera and R. Dias, Response to Comment on "Observation of the Wigner-Huntington transition to metallic hydrogen", Science **357**, eaan2671 (2017).

[9]   B. Li, C. Ji, W. Yang, J. Wang, K. Yang, et al., Diamond anvil cell behavior up to 4 Mbar, P. Natl. Acad. Sci. USA **115**, 1713 (2018).

[10] W. C. Moss, J. O. Hallquist, R. Reichlin, K. A. Goettel, and S. Martin, Finite element analysis of the diamond anvil cell: Achieving 4.6 Mbar. Appl. Phys. Lett. **48**, 1258 (1986).

[11] W. C. Moss and K. A. Goettel, Finite element design of diamond anvils. Appl. Phys. Lett. **50**, 25 (1987).

[12] V. I. Levitas, S. B. Polotnyak, and A. V. Idesman, Large elastoplastic strains and the stressed state of a deformable gasket in high pressure equipment with diamond anvils. Strength Mater. **3**, 221 (1996).

[13] S. Merkel, R. J. Hemley, and H. K. Mao, Finite-element modeling of diamond deformation at multimegabar pressures. Appl. Phys. Lett. **74**, 656 (1999).

[14] B. Feng, V. I. Levitas, and R. J. Hemley, Large elastoplasticity under static megabar pressures: Formulation and application to compression of samples in diamond anvil cells. Int. J. Plast. **84**, 33 (2016).

[15] S. Merkel, R. J. Hemley, H. K. Mao, and D. M. Teter, Finite element modeling and ab-initio calculations of megabar stresses in the diamond anvil cell. Proceedings of the conference AIRAPT-XVII, pp 68-73 (2000).

[16] B. Feng, and V. I. Levitas, Pressure self-focusing effect and novel methods for increasing the maximum pressure in traditional and rotational diamond anvil cells. Sci. Rep. **7**, 45461, (2017)

[17] Novikov N.V., Levitas V.I., Idesman A.V. Theoretical description of thermomechanical effects in high pressure apparatus, High Press. Res. **5**, 868 (1990).

[18] V. I. Levitas and O. M. Zarechnyy, Modeling and simulation of strain-induced phase transformations under compression in a diamond anvil cell. Phys. Rev. B **82**, 174123 (2010).

[19] B. Feng, V. I. Levitas, and Y. Z. Ma, Strain-induced phase transformation under compression in a diamond anvil cell: Simulations of a sample and gasket. J. Appl. Phys. **115**, 163509 (2014).

[20] B. Feng, V. I. Levitas, and O. M. Zarechnyy, Plastic flows and phase transformations in materials under compression in diamond anvil cell: Effect of contact sliding. J. Appl. Phys. **114**, 043506 (2013).

[21] V. I. Levitas and O. M. Zarechnyy, Modeling and simulation of strain-induced phase transformations under compression and torsion in a rotational diamond anvil cell. Phys. Rev. B **82**, 174124 (2010).

[22] B. Feng and V. I. Levitas, Effects of gasket on coupled plastic flow and strain-induced phase transformations under high pressure and large torsion in a rotational diamond anvil cell. J. Appl. Phys. **119**, 015902 (2016).

[23] B. Feng and V. I. Levitas, Coupled phase transformations and plastic flows under torsion at high pressure in rotational diamond anvil cell: Effect of contact sliding. J. Appl. Phys. **114**, 213514 (2013).

[24] B. Feng and V. I. Levitas, Large elastoplastic deformation of a sample under compression and torsion in a rotational diamond anvil cell under megabar pressures. Int. J. Plast. **92**, 79 (2017).

[25] W. A. Bassett, Diamond anvil cell, 50th birthday, High Pressure Res **29**, 163 (2009).

[26] J. M. Lang and Y. M. Gupta, Experimental determination of third-order elastic constants of diamond. Phys. Rev. Lett. **106**, 125502 (2011).

[27] F. D. Murnaghan, Finite deformation of an elastic solid (Wiley, New York, 1951).

[28]   V. I. Levitas, Large Deformation of Materials with Complex Rheological Properties at Normal and High Pressure (Nova Science Publishers, New York, 1996).

[29]   M. H. Manghnan, K. Katahara, and E. S. Fisher, Ultrasonic equation of state of rhenium. Phys. Rev. B **9**, 1421 (1974).

[30]   O. H. Nielsen, Optical phonons and elasticity of diamond at megabar stresses. Phys. Rev. B **34**, 5808 (1986).

[31]   Eremets, M.I., High pressure experimental methods. (Oxford University, Oxford, 1996).

[32]   B. Feng and V. I. Levitas, Coupled elastoplasticity and plastic strain-induced phase transformation under high pressure and large strains: formulation and application to BN sample compressed in a diamond anvil cell. Int. J. Plast. **96**, 156-181 (2017).

[33]   V.I. Levitas, High pressure phase transformations revisited. J. Physics: Condensed Matter, **30**, 163001 (2018).